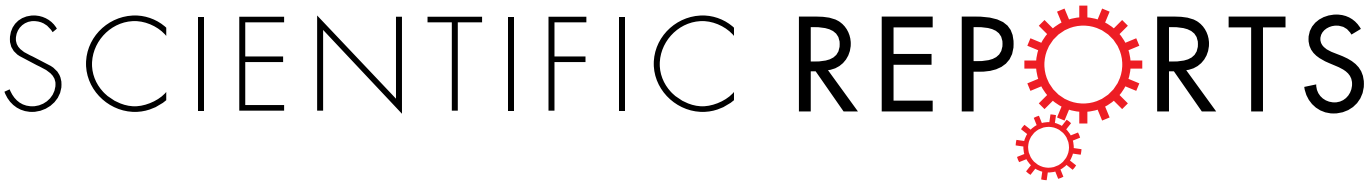

OPEN

Received: 09 June 2016
Accepted: 25 October 2016
Published: 17 November 2016

Tunable high-performance microwave absorption for manganese dioxides by one-step Co doping modification

Guocheng Lv[1], Xuebing Xing[1], Limei Wu[1], Wei-Teh Jiang[2], Zhaohui Li[1,2,3] & Libing Liao[1]

The frequencies of microwave absorption can be affected by the permanent electric dipole moment which could be adjusted by modifying the crystal symmetry of the microwave absorbing materials. Herein, we corroborate this strategy experimentally and computationally to the microwave absorption of manganese dioxides. Nanosized Co-doped cryptomelane (Co-Cryp) was successfully synthesized by a one-step reaction. The introduction of Co(III) induced a change of crystal symmetry from tetragonal to monlclinic, which could lead to an increase of its permanent electric dipole moment. As a result, the frequencies of maximum microwave absorption were regulated in the range of 7.4 to 13.9 GHz with a broadened bandwidths. The results suggested that microwave absorption of manganese dioxides can be tailored with Co doping to expand their potential uses for abatement of various microwave pollutions.

Electromagnetic pollution (EMP) is one of the largest pollution after air, water, and noise pollutions that threaten human's health[1]. Thus, great efforts have been made to alleviate the EMP problem. As such, microwave absorbing materials (MAMs) become one of the hottest topics in the field of materials science for their potential reduction of EMP. In the 1980 s, MAMs made of ferrite were in the center of research focus[2]. The ferrite MAMs were replaced by MAMs made of polycrystalline fibers in America in the 1990s[3]. In the 21st century, nanoscale MAMs turn into a leading research focus in the world[4–8].

Up to now, most of the researches have focused on developing new MAMs and increasing their microwave absorption rate. For example, magnetic nano-composites, such as ZnO/Fe[9], α-Fe_2O_3@$CoFe_2O_4$[10], and Ni/Co[11], were extensively used as MAMs. The multi-walled carbon nanotube coated with CdS nanocrystals was a promising functional material for high temperature microwave absorption[12]. In the syntheses of BaMnZnCo-W ferrite, the influence of Co(II) content on the properties of microwave absorption was observed. At a sample thickness of 2.5 mm, a reflection loss of −40 dB could be achieved at a frequency of 11.5 GHz[13]. For the core-shell $MnFe_2O_4$-TiO_2 nano-composites, their microwave absorbing properties were higher than that of $MnFe_2O_4$ when the permittivity and permeability of the complex $MnFe_2O_4$ and $MnFe_2O$-TiO_2 composites were measured in the microwave frequency ranges of 2–10 GHz[14]. In the 2 to 18 GHz range, 3-D Fe_3O_4 nanocrystals and multi-walled carbon nanotubes could enhance microwave absorption with tunable strong-absorption wavebands[15]. As a highly effective microwave absorption material, the Fe_3O_4/multi-walled carbon nanotubes are effective fillers for electromagnetic shielding and attenuation[16]. High-efficiency electromagnetic interference shielding could be achieved at elevated temperature using chemically graphitized r-GOs[17].

However, the microwave absorption frequencies of all the MAMs mentioned above were not adjustable. Fewer studies were focused on regulating microwave absorption frequencies of the MAMs. Materials with high strength and adjustable absorption frequencies and bandwidth should have attracted more attention. The frequency that has the highest response to microwave absorption is the inherent property of the materials, which could be manipulated by controlling the crystal structure and morphology of the materials[18,19]. Because the basic

[1]Beijing Key Laboratory of Materials Utilization of Nonmetallic Minerals and Solid Wastes, National Laboratory of Mineral Materials, School of Materials Science and Technology, China University of Geosciences, Beijing 100083, PR China. [2]Department of Earth Sciences, National Cheng Kung University, Tainan, 70101, Taiwan. [3]Geosciences Department, University of Wisconsin – Parkside, Kenosha, WI 53144, USA. Correspondence and requests for materials should be addressed to G.L. (email: guochenglv@cugb.edu.cn) or Z.L. (email: li@uwp.edu)

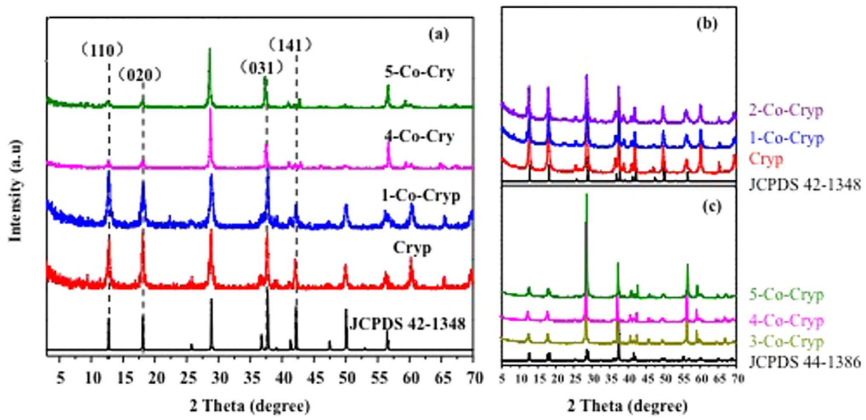

Figure 1. XRD of Co(III)-doped Cryp under different Co(III) concentrations (**a**) matching with monoclinic structure (**b**) and tetragonal structure (**c**).

properties of materials could affect magnetic and dielectric loss when the materials absorb microwave[20], it is worth noting that crystal structure and morphologies are important factors to microwave absorption. In the frequency range of 4–14 GHz more than 99% of EM wave energy was attenuated by a synthesized architecture of Fe_3O_4 nanorod arrays and graphene sheets[8]. Moreover, MnO_2 nanorods prepared with a hydrothermal method reached a minimum reflection loss of 74.1% or −5.9 dB at 7.57 GHz[21].

Manganese dioxides (MOs) have excellent microwave absorption properties. They are made of corner- or edge-sharing [MnO_6] octahedra mostly forming tunnel-like or layered structures[22–23]. Cryptomelane (Cryp) is a type of MOs made of a 2 × 2 tunnel structure. Cryp is able to produce instantaneous polarization and strong activity centre under the action of microwave[24–25], form reactive oxygen species, and have strong responses to microwaves[26]. Furthermore, due to the replacement of Mn(VI) by Mn(III) and Mn(II), charge balance is compensated by K^+ residing in the channels[27]. When different transitional metal ions enter the Cryp structure to substitute for Mn(III), a change of structure, morphology, or other physical properties could occur. Detailed changes could be linked to the types, amounts, and locations of the doped ions[28]. The structure of Co(II) doped Cryp is subject to change depending upon the Co(II) content[29]. With the change of crystal structure, the morphology and frequencies for microwave absorption are expected to change accordingly. In this study, the change of microwave absorption properties after Cryp was doped with different amounts of Co(III) was characterized. A one-step method to synthesis the Co(III) doped Cryp (Co-Cryp) that is able to regulate the microwave absorption frequencies and bandwidth was developed.

Results and discussion

Characterization of Cryp/Co-Cryp structure. The XRD pattern of raw Cryp matched well with the JCPDS 42–1348 (Joint Committee on Powder Diffraction Standards), indicating a tetragonal system with a space group of I4/m (Fig. 1a). The tetragonal structure is made of double chains of edge-sharing [MnO_6] octahedra parallel to the c axis, and takes four such double chains with the same vertex angle forming a 2 × 2 tunnel framework[23,27]. As the amount of Co(III) doping increased, the XRD peaks of Co-Cryp became broader (Fig. 1b), and the structural symmetry changed to monoclinic with its XRD patterns matching well with JCPDS 44–1386 (Fig. 1c) when the amount of Co(III) doping was 3% or more.

Occupancy of Co(III) the Mn sites was confirmed for both tetragonal and monoclinic structures of Co-Cryp in a structure refinement (Fig. 2). Modeling the atomic positions and site occupancies of the two Co-Cryp structures by the Rietveld method resulted in good discrepancy indices of $R_{exp} = 8.14$, $R_{wp} = 11.35$, $R_p = 8.04$, GOF = 1.39 (Table 1) and $R_{exp} = 8.68$, $R_{wp} = 11.93$, $R_p = 7.59$, GOF = 1.37 (Table 2), suggesting a tetragonal cell with 15% (atom) of Co and a monoclinic cell with 31% (atom) of Co, respectively. In fact, element analysis showed the molar ratios of Co(III) doped into Cryp. As the amount of Co(III) doping increased, more Co(III) was incorporated into the Co-Cryp. For 5-Co-Cryp and 4-Co-Cryp, The amounts of Co(III) were 2.5% and 2.1%, respectively (Table 3). As the amount of $CoCl_3$ used in the synthesis of 5-Co-Cryp was two times that for 4-Co-Cryp, the minute difference in Co(III) contents between 5-Co-Cryp and 4-Co-Cryp suggested gradual saturation of Co(III) in 5-Co-Cryp.

The morphology of raw Cryp was nano-fibrous and the particle size was uniform, with a length of tens of micrometers and a diameter about 50 nm (Fig. 3a). As the doping amount of Co(III) increased, aggregates of granular particles micrometers in diameter became dominant (Fig. 3). The diameter of Co-Cryps changed from 50 nm to 860 nm as the amount of Co(III) increased (Fig. 4). In previous studies, the crystal morphology of Cryp changed from nanofibers to short rods or even granules and the degree of partial disorder of the Cryp structure increased[30], as the doping of transition metal ions increased[31–32].

The specific surface area (SSA) of Cryp was determined using fully automatic nitrogen adsorption BET. As the amount of Co(III) doped increased, the SSA became smaller with the SSA of Cryp being 62.0 m^2/g and that of 5-Co-Cryp being 14.9 m^2/g (Fig. 5).

The $Mn2p_{3/2}$ peak was deconvoluated by a multi-component spectral fitting to determine the distribution of various valence states of Mn in Co-Cryp (Fig. 6a–c). With the increase of initial Co input the amount of Mn(II)

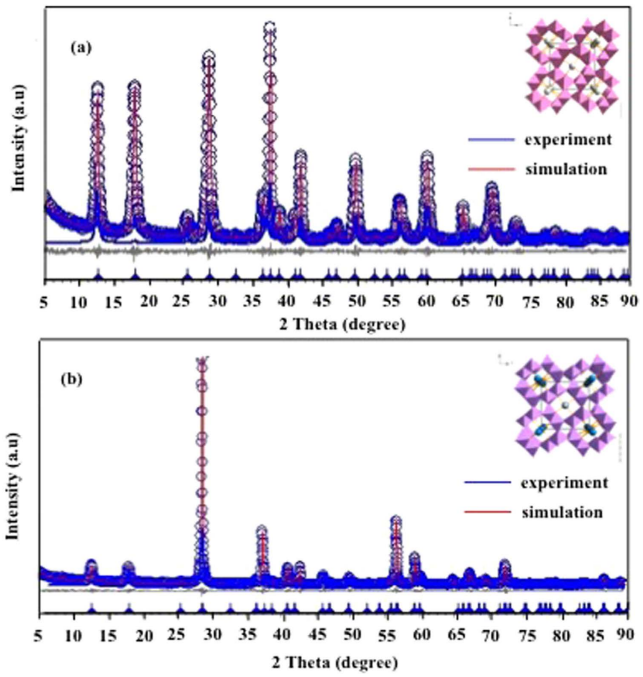

Figure 2. Structural refinement of Cryp with tetragonal symmetry and atomic coordinates (**a**) and monoclinic structure and atomic coordinates (**b**). —— experiment, —— Rietveld simulation.

R_{exp}: 8.14		R_{wp}: 11.35	R_p: 8.04	GOF: 1.39	
R_{exp}': 4.14		R_{wp}': 5.78	R_p' : 4.37	DW: 1.01	
Atom	**Position**	**Occupancy**	**x**	**y**	**z**
K	4	0.33	0	0	0.4959
Co	8	0.15	0.3528	0.1698	0
Mn	8	0.85	0.3528	0.1698	0
O1	8	1	0.1589	0.1825	0
O2	8	1	0.5214	0.1699	0

Table 1. Coordinates and occupancies of atoms in tetragonal Cryp.

R_{exp}: 8.6		R_{wp}: 11.93	R_p: 7.59	GOF: 1.37	
R_{exp}': 6.30		R_{wp}': 8.65	R_p' : 5.66	DW: 1.1	
Atom	**Position**	**Occupancy**	**x**	**y**	**z**
K	4	0.33	0	0.3754	0
Co	8	0.31	0.2837	0	0.0993
Mn	8	0.69	0.2837	0	0.0993
O1	8	1	0.1750	0	0.2282
O2	8	1	0.7925	0	0.3072

Table 2. Coordinates and occupancies of atoms in monoclinic Co-Cryp.

	Co	Mn	O	K
Cryp	0	73.3%	24.3%	2.4%
1-Co-Cryp	0.23%	72.6%	24.6%	2.5%
2-Co-Cryp	0.52%	72.0%	24.7%	2.7%
3-Co-Cryp	1.6%	70.9%	24.7%	2.7%
4-Co-Cryp	2.1%	70.1%	24.8%	2.7%
5-Co-Cryp	2.5%	69.3%	25.4%	2.6%

Table 3. The elements of Co-Cryp by the method of XRF.

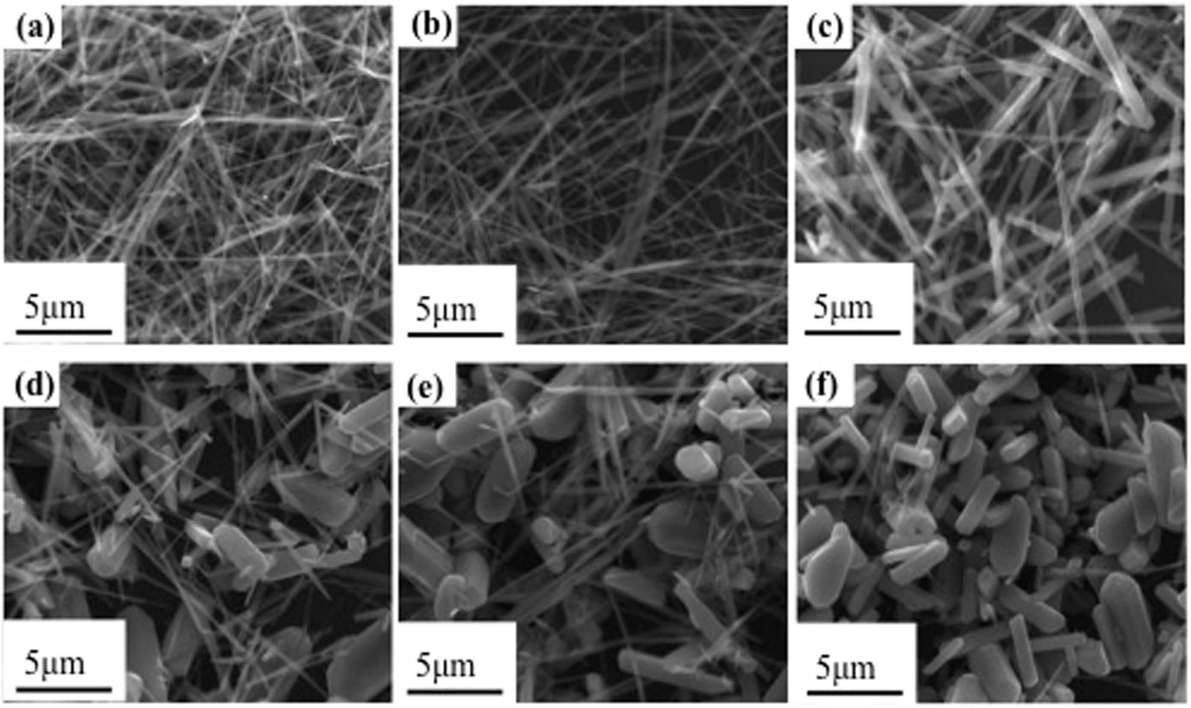

Figure 3. SEM of Cryp doped with different amounts of Co(III) (**a**): for raw Cryp; (**b–f**): for 1, 2, 3, 4 and 5-Co-Cryp.

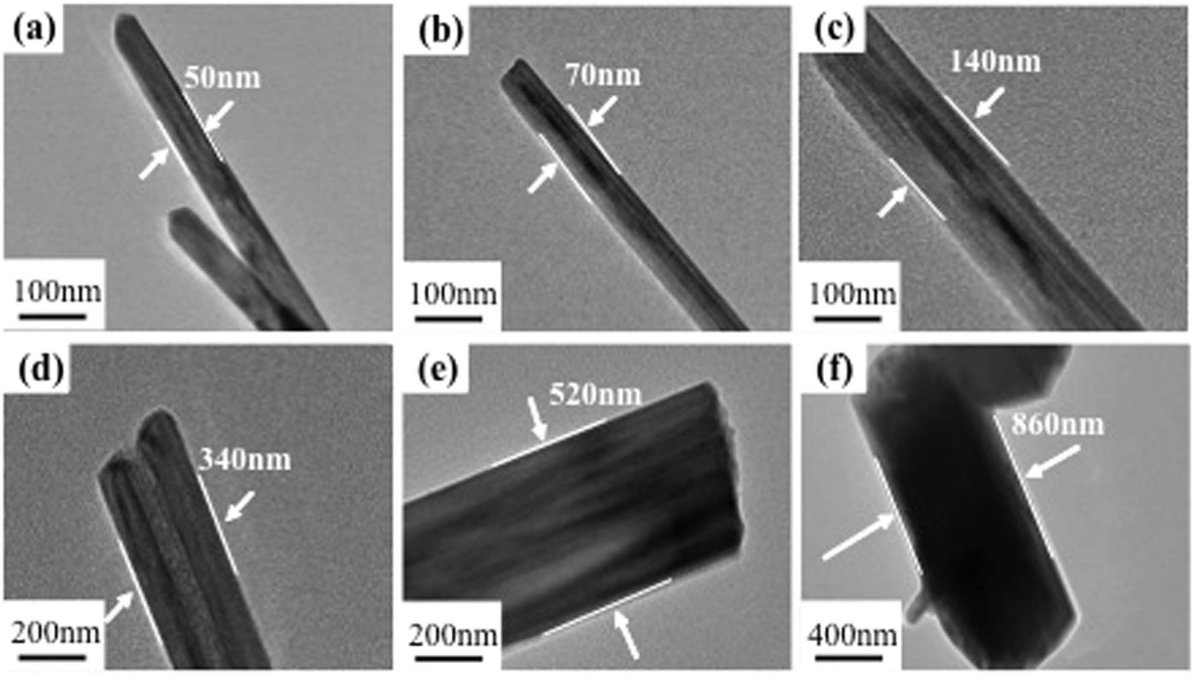

Figure 4. TEM of Cryp doped with different amounts of Co(III) (**a**): for raw Cryp; (**b–f**): for 1, 2, 3, 4 and 5-Co-Cryp.

and Mn(IV) increased while that of Mn(III) decreased (Table 4). The Co(2p) XPS spectra of Co-Cryp showed that the binding energies of $Co(2p_{1/2})$ and $Co(2p_{3/2})$ were ca. 795.5 and 780.5 eV for all of the Co-Cryp samples (Fig. 6d). These values matched well with those of Co(III)[33]. In addition, the split of $Co(2p_{1/2})$ and $Co(2p_{3/2})$ was 15 eV which was nearly identical to that of Co(III) but 1 eV smaller than that of Co(II)[34]. On the contrary, Co(II)

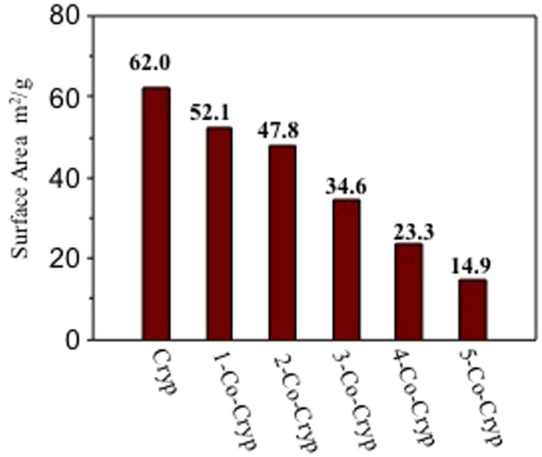

Figure 5. The SSA of Cryp with different amounts of Co(III) doping.

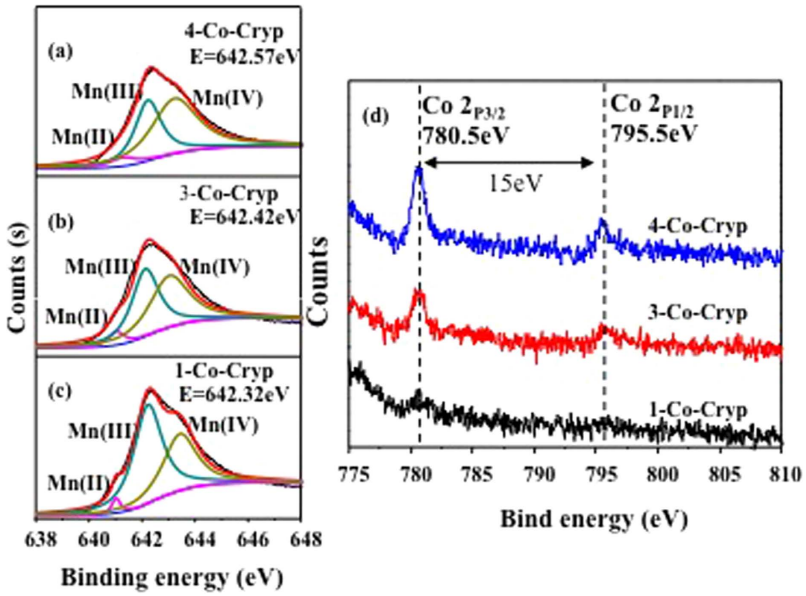

Figure 6. Mn (2p) and Co (2p) XPS spectra of Co-Cryp.

Catalyst	Manganese distribution		
	Mn(II)	Mn(III)	Mn(IV)
1-Co-Cryp	2.57%	58.23%	39.20%
3-Co-Cryp	5.24%	45.36%	49.40%
4-Co-Cryp	5.37%	36.50%	58.13%

Table 4. Results of XPS analysis.

would show an observable satellite feature at 786 eV[35], which is not visible in this study. These features pointed out the presence of Co(III), instead of Co(II), in the crystal structure of Co-Cryp. With Co(III) doping increased, the peak height of Mn(III) decreased accordingly, suggesting substitution of Co(III) for Mn(III) in Co-Cryp. In the preparation of Co-Cryp, Co(II) was oxidized to Co(III) due to the presence of excess Mn(VII) in the reaction. This resulted in substitution of Mn(III) by Co(III) in Co-Cryp, leading to relative increases of the Mn(II) and Mn(IV) signals (Fig. 6), particularly the latter, and thus a rise of the average oxidative state of Mn[36].

Microwave absorption properties of Cryp/Co-Cryp. Magnetic-dielectric composite materials were obtained by scattering Cryp and Co-Cryp particles into paraffin. Compared with metal composites, such Cryp- or

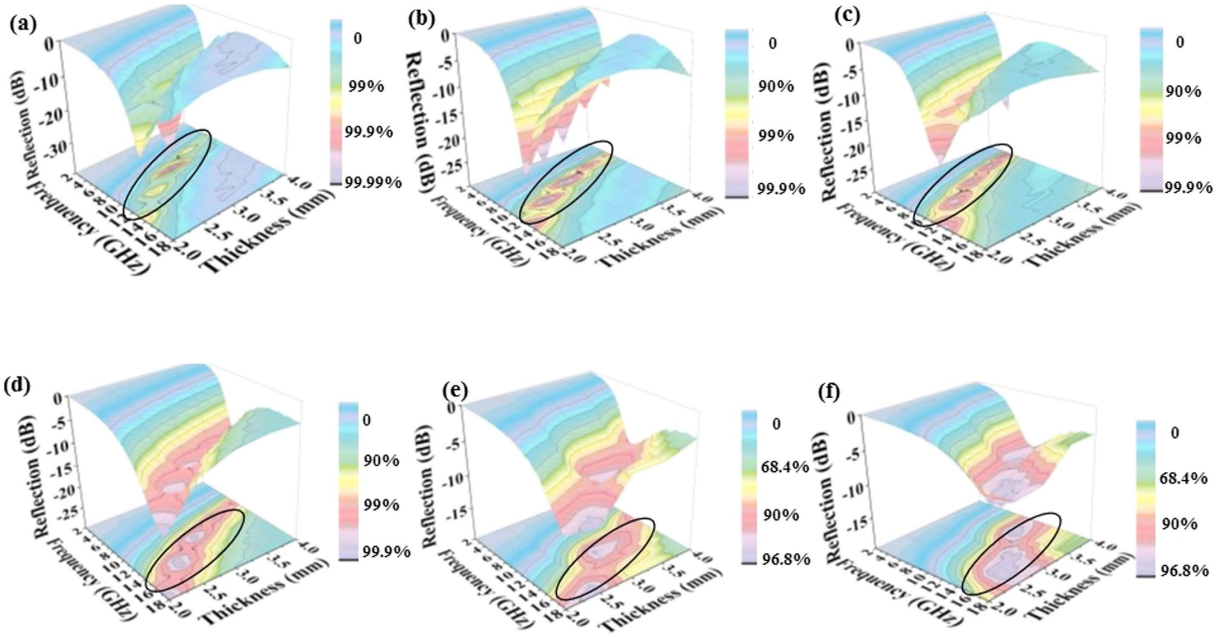

Figure 7. Microwave absorbing properties of Cryp and Co-Cryp. Microwave reflection losses of composites of paraffin and Cryp (**a**) and 1 (**b**), 2 (**c**), 3 (**d**), 4 (**e**), and 5-Co-Cryp (**f**). Specimen thickness was in the range of 2 to 4 mm and the range of microwave frequency was 2–18 GHz.

Co-Cryp/paraffin composites had a higher resistivity. When a fixed amount of EM wave was applied on a material, a small amount of reflected EM wave would indicate an effective attenuation of EM wave energy and the material potentially has a good microwave absorbing property. A smaller coefficient (R) would indicate a larger absorption of the EM wave. The performance of the MAMs can be evaluated by a reflection R defined in the Supplementary Information section.

The reflection losses of Cryp- and Co-Cryp/paraffin composites were calculated from equation 3 (SI) and Cryp/Co-Cryp accounted for 20% and paraffin for 80% of the total losses in Cryp- or Co-Cryp-paraffin composites (Fig. 7). Thus, the maximal attenuation of microwaves by the composites occurred as a function of both specimen thickness and microwave frequency (Fig. 7). With increasing specimen thickness, the maximal attenuation occurred at lower frequency (smaller f_m value) (SI: equation 3). In the thickness range considered, the width of frequency in which maximal microwave attenuation could be achieved by Co-Cryp was much greater than that by Cryp and it shifted towards higher frequency with increasing Co(III) doping. On the other hand, with increasing specimen thickness, the microwave absorption properties also increased.

Changes of EM absorption properties may stem from the phase transition of the MAMs[37–39]. The maximal reflection losses by the Co-Cryp composites mostly had less negative decibel values than −10 dB (i.e., 90% of the incoming power was absorbed), in comparison to −35.4 dB (>99% power absorbed) for the Cryp composite at 3 mm composite thickness (Fig. 7a). An increase of Co(III) doping resulted in a phase transition from tetragonal to monoclinic structure and a decrease (less negative decibel value) of reflection loss and energy absorption (Fig. 8a). However, the frequency and bandwidth for EM attenuation became larger as the Co(III) doping increased (Fig. 8b). This feature suggests potentially broader uses of the functional materials for EMP attenuation[40].

Microwave absorption was attributed to magnetic loss and dielectric loss[41]. Permittivity mainly originates from polarizations of electrons, ions, and intrinsic electric dipoles. Magnetic properties could be affected by crystal structure, special geometrical morphology and size[42–43]. Complex permittivity and complex magnetic permeability of Co-Cryp were analyzed (Fig. 9). The real (ε') and imaginary (ε'') complex permittivity, and the real (μ') and imaginary (μ'') permeability are displayed in Fig. 9a–d. As the amounts of Co(III)-doped increased, the ε' became smaller, suggesting gradual weakening of the dipole polarization and electric polarization of Co-Cryp. Because ε' represents material characterization of polarization. It could clearly be seen the values of ε'' exhibited very complex nonlinear behaviour[44], and also decrease with the increase of Co(III) doping in Cryp. As shown in Fig. 7b, there were relaxations of Cryp. Relaxation I, was located at the frequencies of 7.1, 9.4, and 13.5 GHz for raw Cryp, 1-Co-Cryp, and 2-Co-Cryp, respectively. The relaxation of Cryp was mainly from interfacial polarization and defect dipole polarization[39,45,46]. As the Co(III) doping increased, the frequency of relaxation I shifted to higher frequencies. Compared with the complex permittivity, the changes in complex magnetic permeability were minute and close to zero. Thus, the complex permittivity was the key factor affecting microwave absorption of Cryp.

The change of crystal symmetry and permanent electric dipole moment. The radii of Mn(III) and Co(III) are 0.66 and 0.63 Å. Due to the size difference, the introduction of Co(III) could induce some distortions

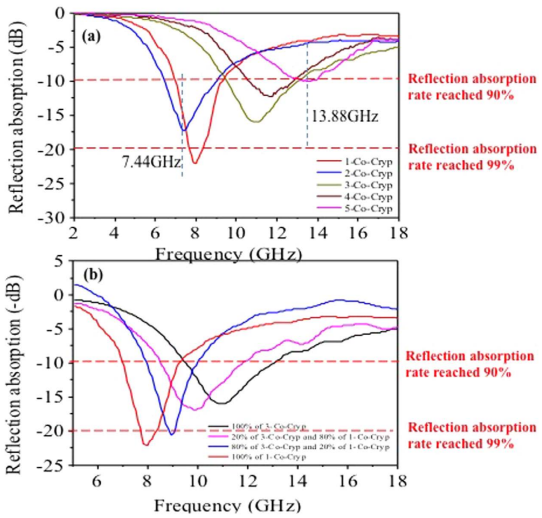

Figure 8. Microwave absorption properties of Cryp doped with different amounts of Co(III) (3 mm thick) (**a**); Microwave absorption properties of the mixture of 1 and 3-Co-Cryp (3 mm thick) (**b**).

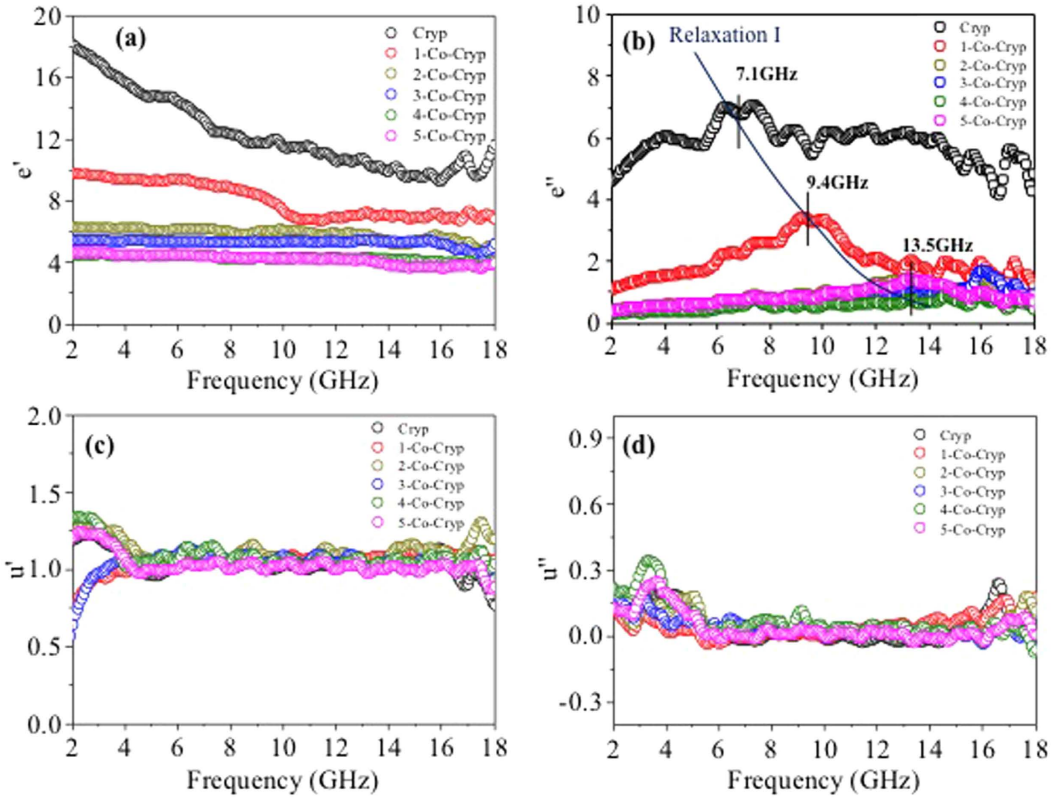

Figure 9. Relative complex permittivity of the real (**a**) and imaginary (**b**) parts and relative complex permeability of the real (**c**) and imaginary parts (**d**) of Cryp doped with different amounts of Co(III) in the frequency range of 2–18 GHz.

Crystal system	a/Å	b/Å	c/Å	β
Cryp-T(I4/m)	9.8401	9.8401	2.8619	90
Cryp-M(C2/m)	9.8317	2.8678	9.8233	90.95

Table 5. The cell parameters of Cryp.

Cryp-T	Unit (nm)			Cryp-M	Unit (nm)		
	a	b	c		a	b	c
Mn	0.8489	0.6700	1.5	Mn	0.1646	0.5	0.34695
O1	0.8350	0.5421	2	O1	0.0423	0	0.3249
O2	0.8350	0.5421	1	O2	0.0423	1	0.3249
O3	0.8456	0.7971	1	O3	0.2947	0	0.3499
O4	0.8456	0.7971	2	O4	0.2947	0	0.3499
O5	0.6545	0.7030	1.5	O5	0.2053	0.5	0.1501
O6	1.0421	0.6650	1.5	O6	0.1561	0.5	0.542
PEDM	d_1	About 0		PEDM	d_2	0.528	
Dipole moment (d*q)		0		Dipole moment (d*q)		$3.3792*10^{-29}$ C·m	

Table 6. The coordinates of atoms and permanent electric dipole moments of Cryp.

in the [MnO_6] octahedra, resulting in a decrease of crystal symmetry from tetragonal to monoclinic[47,48] (Table 5). Accordingly, the anisotropicity increased[20] and the morphology changed from nano-fibers to equidimentsional granules of micrometers in size[49–51] (Figs 3 and 4). Nanosize materials tend to have better microwave absorption properties[52–55]. As evidenced in this work, the nanosize Cryp fibers showed greater EM absorption than the micrometer-sized Co-Cryp.

Moreover, the permanent electric dipole moment increased from 0 to 3.3792×10^{-29} C·m per [MnO_6] octahedron with the increase of anisotropicity (Table 6). The permanent electric dipole moment is closely related to the composite magnetic permeability and complex dielectric constant of materials (Equations 2–4 in SI), and could cause different f_m values and absorption bandwidths[56–59] as is the case in this study. With an increase in the amount of Co(III) doping, a right shift of f_m occurred and the bandwidth of maximal microwave attenuation became significantly larger, albeit with a slight decrease of absorption performance. These features make it optimistic to use Cryp or Co-Cryp as MAMs in a wide range of environments for potential microwave abatement[60–62].

Conclusions

Cryp was demonstrated to be a very good microwave absorption material. The micowave reflection loss of Cryp reached to −35.4 dB. As the amount of Co(III) doped increased, the bandwidth of high attenuation notably expanded and the frequencies shifted significantly to 13.9 GHz. In a nutshell, optimal microwave absorption frequency and bandwidth of Cryp materials can be tuned with a control of crystal structure via selective Co doping.

Experimental Section

Experimental materials. $KMnO_4$, $MnSO_4 \bullet H_2O$, $CoCl_2 \bullet 6H_2O$, diethyl ether, paraffin, and distilled water were purchased from Beijing Chemical Works. All chemicals were analytical grade.

Synthesis of Cryp and Co-Cryp The Cryp samples were produced by the following procedures: 100 mL of 0.1 M $KMnO_4$ and 50 mL of 0.3 M $MnSO_4 \bullet H_2O$ were mixed at room temperature under vigorous stirring for 30 min. Gradually formed brwon precipitates were transferred into a stainless steel autoclave lined with Teflon, and were cured at 140 °C for 24 h. After been being cooled down to room temperature, the precipitates were filtered first, then, washed three times with distilled water and dried at 80 °C for 24 h[63].

The Co-Cryp samples were produced similarly with different quantities of $CoCl_2 \bullet 6H_2O$ added to the $MnSO_4 \bullet H_2O$ solution before being mixed with the $KMnO_4$ solution. During the reaction, Co(II) was oxidized to Co(III) due to an excess amount of Mn(VII) with respect to the reduced amounts of Mn(II) in the reaction.

Preparation of Cryp/Co-Cryp-paraffin composites. The composites for microwave absorption measurement were fabricated by mixing Cryp or Co-Cryp (20%) with paraffin matrix (80%). The mixtures were pressed into a cylindrical shape with Φ_{out} =7.00 mm and Φ_{in} =3.04 mm, respectively. The reflection losses of the composites should be attributed to that of the Cryp or Co-Cryp as the reflection loss of paraffin matrix was similar to that of the air.

Methods of analyses. The powder X-ray diffraction (XRD) patterns of Cryp and Co-Cryp were recorded with a CuKα radiation at 40 kV and 100 mA, a scanning speed of 8° 2θ/min with 0.02° per step. To further investigate the changes in crystal structure of Cryp, Rietveld refinement was performed using the Topaz 3.0 program with the structural parameters of Cryp used as initial parameters.

The purities of the final products were carefully checked by XRD analysis from 5° to 90°. Step scan performed in structural analysis at a rate of 2.35 s/step and a step size of 0.02. TOPAS package was deployed to calculate the structural details in the Rietveld refinement.

Elemental composition of Cryp was determined by X-ray Fluorescence spectrometry (XRF). Micro textures of the Cryp and Co-Cryp precipitates were observed on an FEI Quanta 250 field-emission environmental scanning electron microscope (ESEM) with a voltage of 15 kV. Samples were prepared by drying thick sample suspension on a silicon slide before the ESEM observation. Detailed microstructures and crystallite sizes were analyzed by high-resolution transmission electron microscopy (Model: JEOL JEM-2010F).

An X-ray photoelectron spectroscopy (XPS, Thermo Scientific Co., Ltd.) was used to determine the surface valence of Cryp after being doped with different quantities of Co(III) under a monochromatic CuKα source at 150 W and a base pressure of 6.5×10^{-10} mbar in the measuring chamer.

The permittivity and permeability of the composites were measured by a coaxial wire method in the 2–18 GHz range using a phasor network analyzer PNA N5244A (Agilent).

The formula for the calculation of the geometric centre follows that for the calculation of the permanent electric dipole moment[64].

$$x = \frac{1}{n}\sum x_i,\ y = \frac{1}{n}\sum y_i,\ z = \frac{1}{n}\sum z_i \tag{1}$$

$d = \sqrt{(x_0 - x)^2 + (y_0 - y)^2 + (z_0 - z)^2}$ is the deviation of coordinates of the central atom from the geometric centre. For the $[MnO_6]$ octahedron:

$$Diople - moment = d \times 4 \times 1.60 \times 10^{-19} \times 10^{-11}\ C \cdot m \tag{2}$$

References

1. Ji, W. H., Yang, H. T. & Mandula, H. Research on the electromagnetic pollution. *China Sci. Technol. Overview* **19,** 8–10 (2014).
2. Hirata, A., Matsuyama, S. & Shiozawa, T. Temperature rises in the human eye exposed to EM waves in the frequency range 0.6–6 GHz. *IEEE Trans. Electro. Compat*. **42,** 386–393 (2000).
3. Zhang, Y. *et al.* Broadband and tunable high-performance microwave absorption of an ultralight and highly compressible graphene foam. *Adv. Mater* **27,** 2049–2053 (2015).
4. Jiang, J. T., Wei, X. J., Xu, C. Y., Zhou, Z. X. & Zhen, L. Co/SiO_2 composite particles with high electromagnetic wave absorbing performance and weather resistance *J. Magn. Magn. Mater.* **334,** 111–118 (2013).
5. Li, J. G., Huang, J. J., Qin, Y. & Ma, F. Magnetic and microwave properties of cobalt nanoplatelets. *Mater. Sci. Eng. B*. **138,** 199–204 (2007).
6. Zhang, X. J. *et al.* Enhanced microwave absorption property of reduced graphene oxide (rgo)-$mnfe_2o_4$ nanocomposites and polyvinylidene fluoride. *ACS Appl. Mater. & Inter* **6,** 7471–7478 (2014).
7. Han, Z. *et al.* Broadband electromagnetic-wave absorption by FeCo/C nanocapsules. *Appl. Phys. Lett*. **95,** 023114 (2009).
8. Zhu, C. L. *et al.* Fe_3O_4/TiO_2 Core/Shell Nanotubes: Synthesis and Magnetic and Electromagnetic Wave Absorption Characteristics. *J. Phys. Chem. C*. **114,** 16229–16235 (2010).
9. Liu, X. G., Geng, D. Y., Meng, H., Shang, P. J. & Zhang, Z. D. Microwave-absorption properties of ZnO-coated iron nanocapsules. *Appl. Phys. Lett*. **92,** 173117 (2008).
10. Yan, S. J., Dai, S. L., Ding, H. Y., Wang, Z. Y. & Liu, D. B. Influence of Ni/Co molar ratio on electromagnetic properties and microwave absorption performances for Ni/Co paraffin composites. *J. Magn. Magn. Mater*. **358–359,** 170–176 (2014).
11. Lv, H. L., Liang, X. H., Ji, G. B., Zhang, H. Q. & Du, Y. W. Porous Three-Dimensional Flower-like Co/CoO and Its Excellent Electromagnetic Absorption Properties. *ACS Appl. Mater. & Inter*. **7,** 4744–4750 (2015).
12. Lu, M. M., Wang, X. X., Cao, W. Q., Yuan, J. & Cao, M. S. Carbon nanotube-CdS core-shell nanowires with tunable and high-efficiency microwave absorption at elevated temperature. *Nanotechnology* **27,** 065702 (2016).
13. Cheng, S. H., Hu, G. G. & Luo, M. L. Microwave absorbing properties of BaMnZnCo-W type ferrite. *J Magn. Mater. Devices* **4,** 11–13 (2002).
14. Xiao, H. M., Liu, X. M. & Fu, S. Y. Synthesis, magnetic and microwave absorbing properties of core-shell structured $MnFe_2O_4$/TiO_2 nanocomposites. *Composites Sci. & Tech*. **66,** 2003–2008 (2006).
15. Chen, Y. H. *et al.* 3D Fe_3O_4 nanocrystals decorating carbon nanotubes to tune electromagnetic properties and enhance microwave absorption capacity. *J. Mater. Chem. A* **24,** 12621–12625 (2015).
16. Cao, M. S. *et al.* Ferroferric oxide/multiwalled carbon nanotube vs polyaniline/ferroferric oxide/multiwalled carbon nanotube multiheterostructures for highly effective microwave absorption. *ACS Appl. Mater. & Inter*. **4,** 6948–6955 (2012).
17. Wen, B. *et al.* Reduced graphene oxides: light-weight and high-efficiency electromagnetic interference shielding at elevated temperatures. *Adv. Mater.* **26,** 3484–3489 (2014).
18. Viau, G., Vincent, F. F., Toneguzzo, P., Ravel, F. & Acher, O. Size dependence of microwave permeability of spherical ferromagnetic particles. J. *Appl. Phys*. **81,** 2749–2754 (1997).
19. Zhang, L. Y. *et al.* General Route to Multifunctional Uniform Yolk/Mesoporous Silica Shell Nanocapsules: A Platform for Simultaneous Cancer-Targeted Imaging and Magnetically Guided Drug Delivery. *Chem. Eur. J.* **18,** 12512–12521 (2012).
20. Tabatabaie, F., Fathi, M. H., Saatchi, A. & Ghasemi, A. Effect of Mn–Co and Co–Ti substituted ions on doped strontium ferrites microwave absorption. *J. Alloys Compounds* **474,** 206–209 (2009).
21. Wang, G. S., Nie, L. Z. & Yu, S. H. Tunable wave absorption properties of β-MnO_2 nanorods and their application in dielectric composites. *RSC Adv*. **15,** 6216–6221 (2012).
22. Kang, L. P., Zhang, M. M., Liu, Z. H. & Ooic, K. IR spectra of manganese oxides with either layered or tunnel structures. *Spectrochim Acta A*. **67,** 864–869 (2007).
23. Turner, S. & Buseck, P. R. Todorokites: A new family of naturally occurring manganese oxides. *Sci*. **212,** 1024–1027 (1981).
24. Wang, H. C., Liang, H. S. & Chang, M. B. Chlorobenzene oxidation using ozone over iron oxide and manganese oxide catalysts. *J. Hazard. Mater.* **186,** 1781–1787 (2011).
25. Karami, C. *et al.* A novel method for synthesis of cobalt manganese oxide nano catalysts as a recyclable catalyst for the synthesis of some bis (indolyl) methane derivatives. *Catal. Commun*. **27,** 92–96 (2012).
26. Huang, G. Y., Zhao, L., Dong, Y. H. & Zhang, Q. Remediation of soils contaminated with polychlorinated biphenyls by microwave-irradiated manganese dioxide. *J. Hazard. Mater.* **186,** 128–132 (2011).
27. Cai, J., Liu, J., William, S. W. & Steven, L. S. Framework doping of iron in tunnel structure cryptomelane. *Chem. Mater*. **13,** 2413–2422 (2001).
28. Cai, J., Liu, J. & Suib, S. L. Preparative parameters and framework dopant effects in the synthesis of layer-structure birnessite by air oxidation. *Chem. Mater*. **14,** 2071–2077 (2002).
29. Lee, S. H., Kim, T. W., Park, D. H., Choy, J. H. & Hwang, S. J. Single-Step Synthesis, Characterization, and Application of Nanostructured $K_xMn_{1-y}Co_yO_{2-\delta}$ with Controllable Chemical Compositions and Crystal Structures. *Chem. Mater.* **19,** 5010–5017 (2007).
30. Queirós, C. *et al.* The influence of the amide linkage in the Fe(III)-Binding properties of catechol-modified rosamine derivatives. *Chem. Eur. J*. **21,** 15692–15704 (2015).
31. Yoo, H. N., Park, D. H. & Hwang, S. J. Effects of vanadium-and iron-doping on crystal morphology and electrochemical properties of ID nanostructured manganese oxide. *J. Power Sources* **182,** 1374–1379 (2008).

32. Jothiramalingam, R., Viswanathan, B. & Varadarajan, T. K. Preparation, characterization and catalytic properties of cerium incorporated porous manganese oxide OMS-2 catalysts. *Catal. Commun.* **1,** 41–45 (2005).
33. Li, H. *et al.* Structure and properties of Co-doped cryptomelane and its enhanced removal of Pb^{2+} and Cr^{3+} from wastewater. *J. Environ. Sci.* **34,** 77–85 (2015).
34. Yin, H. *et al.* Effects of Co and Ni co-doping on the structure and reactivity of hexagonal birnessite. *Chem. Geol.* **381,** 10–20 (2014).
35. Edla, R. *et al.* Enhanced H_2 production from hydrolysis of sodium borohydride using Co_3O_4 nanoparticles assembled coatings prepared by pulsed laser deposition. *Appl. Catal. A: General*, **515,** 1–9 (2016).
36. Polverejan, M., Villegas, J. C. & Suib, S. L. Higher valency ion substitution into the manganese oxide framework. *J. AM. Chem. Soc.* **126,** 7774–7775 (2004).
37. Bowler, N. Designing dielectric loss at microwave frequencies using multi-layered filler particles in a composite. *IEEE Trans. Dielectr. Electr. Insul.* **13,** 703–711 (2006).
38. Tanaka, T., Montanari, G. C. & Mulhaupt, R. Polymer nanocomposites as dielectrics and electrical insulation-perspectives for processing technologies, material characterization and future applications. *IEEE Trans. Dielectr. Electr. Insul.* **11,** 763–784 (2004).
39. Li, Y., Cao, W. Q., Yuan, J., Wang, D. W. & Cao, M. S. Nd doping of bismuth ferrite to tune electromagnetic properties and increase microwave absorption by magnetic–dielectric synergy. *J. Mater. Chem. C.* **3,** 9276–9282 (2015).
40. Liu, J. W. *et al.* Hierarchical Fe_3O_4@ TiO_2 Yolk–Shell microspheres with enhanced microwave-absorption properties. *Chem. Eur. J.* **19,** 6746–6752 (2013).
41. Chen, T. G. *et al.* Hexagonal and cubic Ni nanocrystals grown on graphene: phase-controlled synthesis, characterization and their enhanced microwave absorption properties. *J. Mater. Chem* **22,** 15190–15197 (2012).
42. Wen, H. *et al.* Hierarchical three-dimensional cobalt phosphate microarchitectures: large-Scale solvothermal synthesis, characterization, and magnetic and microwave absorption properties. *J. Phys. Chem. C* **112,** 15948–15955 (2008).
43. Sun, G., Zhang, X., Cao, M., Wei, B. Q. & Hu, C. W. Facile synthesis, characterization, and microwave absorbability of CoO nanobelts and submicrometer spheres. *J. Phy. Chem. C* **113,** 6948–6954 (2009).
44. Chen, D. Z. *et al.* Controllable fabrication of mono-dispersed RGO-hematite nanocomposites and their enhanced wave absorption properties. *J. Mater. Chem. A* **1,** 5996–6003 (2013).
45. Yang, H. J. *et al.* NiO hierarchical nanorings on SiC: enhancing relaxation to tune microwave absorption at elevated temperature. *ACS Appl. Mater. & Inter.* **7**, 7073–7077 (2015).
46. Liu, J. *et al.* Enhanced permittivity and multi-region microwave absorption of nanoneedle-like ZnO in the X-band at elevated temperature. *J. Mater. Chem. C* **3,** 4670–4677 (2015).
47. Calvert, C. *et al.* Synthesis, characterization, and rietveld refinement of tungsten-framework-doped porous manganese oxide (K-OMS-2) material. *Chem. Mater.* **20,** 6382–6388 (2008).
48. Chen, J. L., Li, J., Huang, X. M. & Shen, W. J. Facile synthesis of Ag–OMS-2 nanorods and their catalytic applications in CO oxidation. *Micropor Mesopor Mat.* **116,** 586–592 (2008).
49. Ding, Y., Xiong, X., Zou, J. P., Zeng, L. & Tu, M. J. Control of morphology and structure for β-Co nanoparticles from cobalt oxalate and research on its phase-change mechanism. *J. Alloy. Compd.* **618,** 497–503 (2015).
50. Knutsson, J. V. *et al.* Atomic scale surface structure and morphology of InAs nanowire crystal superlattices: the effect of epitaxial overgrowth. *ACS Appl. Mater. Interfaces* **7**, 5748–5755 (2015).
51. Cargnello, M. *et al.* Structure, morphology and catalytic properties of pure and alloyed Au–ZnO hierarchical nanostructures. *RSC Adv.* **5,** 41920–41922 (2015).
52. Zhao, B., Shao, G., Fan, B. B., Zhao, W. Y. & Zhang, R. Facile synthesis and enhanced microwave absorption properties of novel hierarchical heterostructures based on a Ni microsphere–CuO nano-rice core–shell composite. *Phys. Chem. Chem. Phys.* **17,** 6044–6052 (2015).
53. Yu, M., Yang, P. G., Fu, J. & Liu, S. Z. Flower-like carbonyl iron powder modified by nanoflakes: Preparation and microwave absorption properties. *Appl. Phys. Lett.* **106,** 161904 (2015).
54. Wu, H. J. *et al.* Co^{2+}/Co^{3+} ratio dependence of electromagnetic wave absorption in hierarchical $NiCo_2O_4$–$CoNiO_2$ hybrids. *J. Mater. Chem. C.* **3,** 7677–7690 (2015).
55. Reshi, H. A. *et al.* Nanostructured $La_{0.7}Sr_{0.3}MnO_3$ compounds for effective electromagnetic interference shielding in the X-band frequency range. *J. Mater. Chem. C.* **3,** 820–827 (2015).
56. Cheng, Z. X. *et al.* Aromatic poly (arylene ether urea) with high dipole moment for high thermal stability and high energy density capacitors. *Appl. Phys. Lett.* **106,** 202902 (2015).
57. Wei, J. J. *et al.* Achieving high dielectric constant and low loss property in a dipolar glass polymer containing strongly dipolar and small-sized sulfone groups. *ACS Appl. Mater. & Inter.* **7,** 5248–5257 (2015).
58. Hopkins, B. *et al.* Interplay of magnetic responses in all-dielectric oligomers to realize magnetic fano resonances. *ACS Photonics* **2,** 724–729 (2015).
59. Zheng, X. L. *et al.* Hydrophobic graphene nanosheets decorated by monodispersed superparamagnetic Fe_3O_4 nanocrystals as synergistic electromagnetic wave absorbers. *J. Mater. Chem. C.* **3,** 4452–4463 (2015).
60. Torchinsky, D. H. *et al.* Structural distortion-induced magnetoelastic locking in Sr_2IrO_4 revealed through nonlinear optical harmonic generation. *Phy. Review Lett.* **114,** 096404 (2015).
61. Nakajima, T. *et al.* Uniaxial-stress control of spin-driven ferroelectricity in multiferroic $Ba_2CoGe_2O_7$. *Phy. Review Lett.* **114,** 067201 (2015).
62. Jiang, X. X. *et al.* The role of dipole moment in determining the nonlinear optical behavior of materials: ab initio studies on quaternary molybdenum tellurite crystals. *J. Mater. Chem. C* **2,** 530–537 (2014).
63. Gao, T. *et al.* Microstructures and spectroscopic properties of cryptomelane-type manganese dioxide nanofibers. *J. Phys. Chem. C.* **112,** 13134–13140 (2008).
64. Wang, X. Y. *et al.* Mechanism and process of methylene blue degradation by manganese oxides under microwave irradiation. *Appl. Catal. B: Environ.* **160–161,** 211–216 (2014).

Acknowledgements

This research was finaicailly supported by: (1) Beijing Natural Science Foundation (2153041); (2) MOST 104–2811-M-006-001 and 104-2116-M-006-011 from the Ministry of Science and Technology, Taiwan, to Jiang; (3) The International S & T Cooperation (S2014ZR0062); and (4) The Fundamental Research Funds for the Central Universities (53200859448).

Author Contributions

G.C. Lv and Z.H. Li conceived and designed the experiments. X.B. Xing and L.M. Wu carried out the experiments. W. Jiang and L.B. Liao analyzed the data. All authors discussed the results. G.C. Lv, Z.H. Li, X.B. Xing and L.M. Wu wrote the paper. The manuscript has been reviewed and approved by all authors.

Additional Information

Supplementary information accompanies this paper at http://www.nature.com/srep

Competing financial interests: The authors declare no competing financial interests.

How to cite this article: Lv, G. *et al.* Tunable high-performance microwave absorption for manganese dioxides by one-step Co doping modification. *Sci. Rep.* **6**, 37400; doi: 10.1038/srep37400 (2016).

Publisher's note: Springer Nature remains neutral with regard to jurisdictional claims in published maps and institutional affiliations.